The Astrophysical Journal, 942:38 (11pp), 2023 January 1 https://doi.org/10.3847/1538-4357/aca415

Locating Type II-P Supernovae Using the Expanding Photosphere Method. I. Comparing Distances from Different Line Velocities

R. C. Mitchell[1], B. Didier[2], S. Ganesh[3], K. Acharya[4], R. Khadka[5], and B. Silwal[6]
[1] St. Ambrose University, Davenport, IA 52803, USA; mitchellrobertc@sau.edu
[2] Katherine Shaw Bethea Hospital, Dixon, IL 61021, USA
[3] Lockheed Martin Space Systems Company, Titusville, FL 32780, USA
[4] Knapheide Manufacturing Company, Quincy, IL 62305, USA; ka028m@knapheide.com
[5] Phillips-Medisize, Hudson, WI 54016, USA
[6] Dell Technologies, Round Rock, TX 78682, USA
Received 2021 October 29; revised 2022 November 1; accepted 2022 November 11; published 2023 January 6

Abstract

W present the results of our work testing a version of the Expanding Photosphere Method (EPM) used by Hamuy et al. and Dessart & Hillier to calculate distances to Type II-P supernovae, accounting for the deviations of their luminosities from those of true blackbodies. This method was applied to a sample of supernovae with data sets covering different postexplosion time periods. Different spectral lines in visible wavelengths—Hβ, He I, Fe II, Sc II, Na I, and Ba II—are used to measure the expansion velocity with the goal of determining the species that produces the most reliable distance determination when combined with the blackbody temperature of the effective photosphere. This research suggests that Hβ, Fe II, and Ba II lines are most likely to yield accurate distances when combined with blackbody temperature, and provides further evidence of EPM's effectiveness as an indicator of distance, provided we have a minimum of three data sets covering a broad range of postexplosion phases of the supernova.

Unified Astronomy Thesaurus concepts: Type II supernovae (1731); Spectral line identification (2073); Effective temperature (449); Galaxy distances (590); Baade-Wesselink method (131); Radial velocity (1332)

1. Type II-P Supernovae

A Type II-P supernova (SN) is theorized to be the explosion of a red supergiant star that still retains a thick hydrogen envelope (Filippenko 1997; Smartt et al. 2009; Smartt 2015). Early-time II-P continuum spectra generally approximate a single-temperature Planck function from UV to IR wavelengths (Filippenko 1997). The temperature falls steadily until it reaches the hydrogen-recombination temperature, 5000–6000 K, around 3–4 weeks after the explosion. From there, the photosphere is defined by the hydrogen-recombination front that gradually recedes through the envelope and releases shock-deposited energy, thus maintaining a roughly constant temperature for two or more months during the "plateau" phase (Schmidt et al. 1992; Filippenko 1997; see Section 2.2).

SNe II-P come from massive, short-lived stars, and can potentially outshine their host galaxies. Such massive stars are theorized to have been among the first generation of stars, perhaps forming no more than 200 million years after the Big Bang, corresponding to $z > 15$. An accurate method of measuring distances to SNe II-P would therefore constrain the value of the Hubble constant and other cosmological parameters much closer to the origin of the universe than through the use of Type Ia SNe (SNe Ia). Although often favored as cosmological standard candles, observations and models of SNe Ia tell us that most are the detonations of evolved white dwarfs. Therefore, we do not expect them to have occurred until at least a billion years after the Big Bang ($z \leqslant 5$).

The Expanding Photosphere Method (EPM) has been used for decades to measure distances to SNe II (Kirshner & Kwan 1974). The method relies on determining the temperature of the ejecta's photosphere, often by fitting a blackbody curve to the continuum spectrum, and the velocity of its expansion. The photosphere's expansion velocity can be calculated from the Doppler blueshift of an absorption line that forms at the photosphere. Blended or misidentified lines can distort the calculation of photosphere velocity or increase its uncertainty; therefore, this part of the calculation requires an easily identified, isolated line or set of lines. A general trend has been observed that stronger lines show higher velocities, most likely due to their larger optical depths (Hamuy et al. 2001; Leonard et al. 2002b). This is particularly true for the Hα line, which in previous studies consistently showed velocities considerably higher than other, weaker lines like Fe II and Sc II (Jeffery & Branch 1989; Hamuy et al. 2001; Spiro et al. 2014).

Other studies generally favor using Fe II λ4924/5018/5169 (Leonard et al. 2002b; Bose & Kumar 2014). Some use an average of all metal lines except the very strong Ca H and K (Eastman & Kirshner 1989; Schmidt et al. 1994), while others have used only the 5169 feature (Gall et al. 2018; Van Dyk et al. 2019; Dong et al. 2021). The disadvantage is that these lines cannot be used for early-time spectra, and studies of synthetic spectra question their accuracy (Jones et al. 2009). Eastman & Kirshner (1989) suggested using Balmer line velocities corrected for the ratio of H-to-Fe velocities when the Fe lines first become visible. Atmospheric models suggest the Hβ line forms close to the photosphere (Jones et al. 2009). Other sources use a ratio of Hβ-to-Fe II λ5169 velocities determined by Nugent et al. (2006). Takats & Vinko (2012)

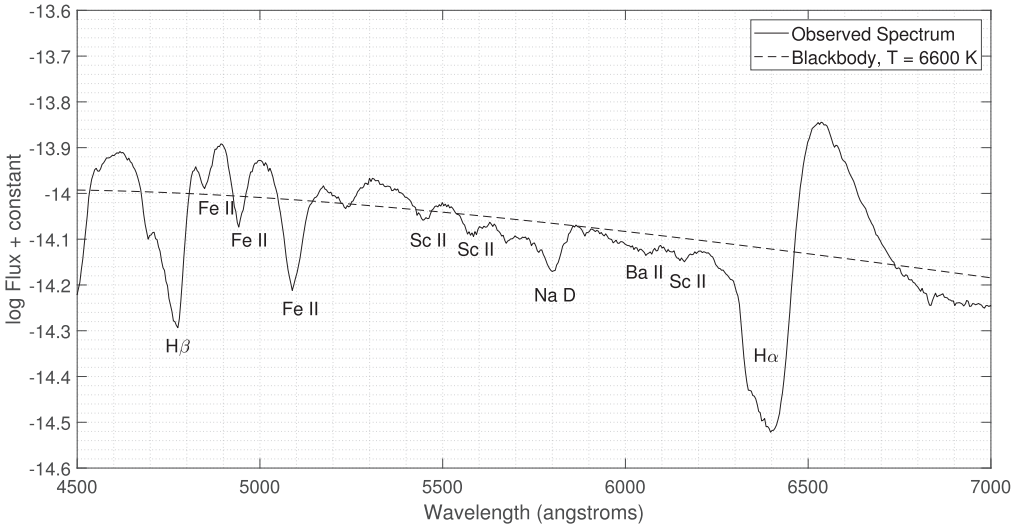

Figure 1. Spectrum of the 2012 September 9 visible spectrum of SN 2012ec, 37 days postexplosion, with a sample of prominent lines identified. Note the weakness of the Ba II 6142 and Sc II 6246 lines. Since this is 37 days postexplosion, we assume the feature at λ5800 is Na D rather than He I.

Table 1
Species for Line Velocities

Species	Wavelengths (Å)
Hβ	4861
He I	4472/5876/7065/7281
Na I D	5890/5896
Sc II	5526/5658/6246
Fe II	4924/5018/5169
Ba II	4554/5854/6142

offer a discussion of the reliability of different line species for photospheric velocity determination.

For this study, we used EPM to calculate the distances to a sample of SNe, using the velocities derived from several different line species listed in Table 1, and compared the distances from different line velocities to each other. If a species has multiple lines, an average velocity was derived from all resolvable lines given for it in the table. Figure 1 is an example from our spectrum sample, showing line identification and the best-fit blackbody temperature curve.

Section 2 of this article details the computations and limitations of EPM. Section 3 discusses how we selected SNe for our sample and the data necessary from each SN and its host galaxy for EPM calculations. Section 4 details how temperatures and expansion velocities of SN photospheres are determined in this study. Results of our study are analyzed in Section 5 and summarized in Section 6.

2. Expanding Photosphere Method

2.1. Angular versus Linear Radius

EPM is a variation of the Baade–Wesselink method (Baade 1926; Kirshner & Kwan 1974), comparing an SN photosphere's angular radius θ to its linear radius R to calculate its distance d. This is a direct geometric calculation of the photosphere's angular radius, independent of other methods on the distance ladder.

If we assume that the SN envelope expands freely, then R is simply a linear function of time and its expansion velocity v; therefore,

$$\theta = \frac{R}{d} = \frac{v(t-t_0)}{d(1+z)}, \quad (1)$$

where t_0 is the explosion epoch. The $(1+z)$ factor comes from relativistic time dilation stretching the observed time t–t_0 necessary for the ejecta to reach R for a given v (Schmidt et al. 1994). This last correction will be especially important when applying the EPM to SNe at cosmological distances; the larger the host-galaxy redshift, the larger the time dilation correction. SNe II-P have been spectroscopically confirmed at redshifts out to $z = 0.335$ (Gall et al. 2018), and deep sky surveys such as the Rubin Observatory's Legacy Survey of Space and Time (LSST) anticipate detection of SNe out to $z \geqslant 3$ (Petrushevska 2020). Yan et al. (2023) reported that the James Webb Space Telescope detected candidate galaxies at $z > 11$, possibly up to 20.

Equation (1) assumes that the radius of the original star is negligible compared to R, an assumption that may be considered valid for red supergiant progenitors at all but the first few days after explosion (Schmidt et al. 1992; Hamuy et al. 2001).

If t_0 is known precisely, then the distance can be calculated from θ and v at any time t. If t_0 is not precisely known, the equation is rewritten as

$$t = \left(\frac{\theta}{v}\right)(1+z)d + t_0. \quad (2)$$

This defines an xy-graph of time versus θ/v, with a slope of $(1+z)d$ and a y-intercept of t_0; therefore, the distance is derived using multiple determinations of θ and $v_{\rm phot}$ at different epochs (Leonard et al. 2002b).

2.2. EPM Assumptions

To derive θ, we first make three assumptions:

1. *The SN envelope has a thin photosphere.* This assumption is largely valid for hydrogen-rich Type II-P SNe during the plateau phase, when the ejecta is optically thick (Vinkó & Takáts 2007) and the hydrogen-recombination

Table 2
Data on Supernovae used in this Study

SN	Host Galaxy	z	t_0 (JD 2,400,000)	Total E_{B-V}	Photometry Sources
1999em	NGC 1637	0.00239	51,478.8 ± 1	0.1	H01; Leonard et al. (2002b)
1999gi	NGC 3184	0.00198	$51{,}518.3^{+3.0}_{-3.1}$	0.21 ± 0.09	Leonard et al. (2002a)
2002gd	NGC 7537	0.00892	52,552 ± 2	0.078	Spiro et al. (2014)
2004et	NGC 6946	0.00013	53,270.5	0.41	Sahu et al. (2006)
2006bp	NGC 3953	0.00351	53,834.2(1)	0.4	Dessart et al. (2008)
2009N	NGC 4487	0.00346	54,848.1	0.13 ± 0.02	Takats et al. (2014)
2012ec	NGC 1084	0.00469	56,143.5	0.144	Barbarino et al. (2015)
2013ab	NGC 5669	0.00456	56,340.0 ± 1.0	0.055 ± 0.055	Bose et al. (2015)
2013fs	NGC 7610	0.01185	56,571.12 ± 0.5	0.04	Valenti et al. (2016)
2017eaw	NGC 6946	0.00013	57,885.7 ± 0.1	0.41 ± 0.1	Szalai et al. (2019)

Reference. (1) Quimby et al. (2007).

front dominates the emergent flux (Filippenko 1997; Hamuy et al. 2001). Dessart & Hillier (2005) and Dessart et al. (2015) noted that UV line blanketing increases the radius of the effective photosphere more so for shorter wavelengths than longer, thus effectively widening the photosphere and invalidating this assumption beyond the plateau phase.

2. *The SN envelope is spherically symmetric.* There are two possible sources of asymmetry: asymmetry in the progenitor and asymmetry in the explosion (e.g., bipolar outflow due to jets or impedance from circumstellar rings). Most red supergiant progenitors are unlikely to have asymmetries significant enough to affect EPM results (Schmidt et al. 1992). Polarization, indicating asymmetry in the ejecta, has been detected in some SNe II-P, e.g., 2004dj (Leonard et al. 2006) and 2017gmr (Nagao et al. 2019), and Wang & Wheeler (2008) noted that many core-collapse SNe show asphericity at least in the inner layers of the ejecta. Leonard et al. (2006) noted that significant polarization did not appear in 2004dj's spectrum until at least 90 days after the explosion. Maeda et al. (2002) and Couch et al. (2009) further stated that although shock fronts propagate laterally through the core, they ultimately become completely spherical through the hydrogen envelope. This supports the theory that any significant asymmetries in an SN II-P are confined to the innermost regions of the ejecta.
3. *The SN photosphere is a diluted blackbody.* As stated in Leonard et al. (2002b), conservation of flux from a spherically symmetric blackbody requires

$$4\pi R^2 \pi B_\lambda(T) = 4\pi d^2 f_\lambda. \tag{3}$$

This results in the following expression for θ:

$$\theta = \frac{R}{d} = \left[\frac{f_\lambda}{\pi B_\lambda(T)}\right]^{0.5}, \tag{4}$$

where f_λ is the observed flux at wavelength λ, and $B_\lambda(T)$ is the Planck function at λ of a blackbody of surface temperature T. SNe II have scattering-dominating atmospheres, causing the emergent flux to be less than that of a perfect blackbody with the same radius and temperature (Schmidt et al. 1992). Dividing the right side of Equation (4) by a *flux dilution factor* ζ corrects for this deviation. Factoring in additional corrections for extinction A and the host galaxy's redshift z (Leonard et al. 2002b; Dessart & Hillier 2005), the expression for angular radius then becomes

$$\theta = \frac{R}{d} = \left[\frac{f_\lambda(1+z)}{10^{-0.4A_\lambda}\zeta^2_{\lambda'}\pi B_{\lambda'}(T)}\right]^{0.5}, \tag{5}$$

$$\lambda' = \frac{\lambda_{\rm obs}}{1+z}. \tag{6}$$

Transforming this equation using the logarithmic observed magnitude scale m,

$$\log\theta = -\log\zeta_{\lambda'} - 0.2(m_\lambda - A_\lambda - b_{\lambda'}) + 0.5\log(1+z), \tag{7}$$

$b_{\lambda'}(T)$ is the synthetic magnitude at wavelength λ' of the Planck function for temperature T. Both b and ζ are expressed as temperature-dependent polynomial relations in the temperature range $4000 < T < 25{,}000$ K:

$$b_\lambda(T) = \sum_{i=0}^{5} c_{i,\lambda}\left(\frac{10^4 K}{T}\right)^i, \tag{8}$$

$$\zeta_{\lambda'}(T) = \sum_{i=0}^{2} a_i\left(\frac{10^4 K}{T}\right)^i. \tag{9}$$

Hamuy et al. (2001, hereafter H01) empirically derived a_i and $c_{i,\lambda}$ coefficients for these relations; their $c_{i,\lambda}$ coefficients were modifications of those from Eastman et al. (1996, hereafter E96). Dessart & Hillier (2005, hereafter D05) derived an alternate set of $c_{i,\lambda}$ coefficients using different atmospheric models. It should be noted that both models for determining ζ were calculated specifically for hydrogen-rich Type II-P SNe. Spectrophotometry of other SN types can be dominated by other elements whose opacities are not as well understood as hydrogen; hence, the amount by which they deviate from being perfect blackbodies is more difficult to model (Eastman et al. 1996).

The angular radius of the photosphere can therefore be calculated from the host galaxy's redshift, the observed color magnitude, the extinction and flux dilution factors in the same passband, and the Planck function for the photosphere's temperature. Uncertainty in the distance is calculated as a Gaussian propagation of the uncertainties in redshift, temperature, line velocity, color magnitudes, and extinction.

Studies recommend limiting the time period for EPM calculations to no more than 50 days postexplosion, due to departure from linearity in θ/v (Jones et al. 2009) or to increasing uncertainties in ζ as T decreases (D05). For our first

run of calculations, we adhered strictly to this 50 day limit, measuring from the estimated explosion epochs given in the sources in Table 2, with exceptions described in Section 3.

3. Data

We restricted our sample of SNe to Type II-P, as identified in the Weizmann Interactive Supernova Data Repository (WISeREP[7]; Yaron & Gal-Yam 2012), the Open Supernova Catalog (OSC[8]; Guillochon et al. 2017), and in other literature searches. Further restrictions to our sample were based on the availability and quality of spectra and *BVRI*-color photometry over a wide range of epochs, and for a lack of any published evidence of significant asphericity in the envelope. Spectra were obtained from WISeREP and OSC. Host galaxy redshifts were obtained from the NASA/IPAC Extragalactic Database (NED[9]). Photometry, estimated explosion epochs, and extinctions A were obtained from published sources specific to each of the SNe. If published sources only provide E_{B-V} for the extinction, we use the reddening law of Fitzpatrick (1999) to estimate A_V, A_R, and A_I, and the Burstein–Heiles law (Burstein & Heiles 1982) to estimate A_B.

To date, this has given us a sample of 10 SNe, 3 of which (SN 2002gd, SN 2012ec, and SN 2013fs) have no previously published EPM distances. For each available spectrum, there must also be photometry available for the same epoch, forming what will hereafter be known as a spectrophotometry set. We accepted photometry whose dates were no more than one day off the nearest available spectrum. For each line used to calculate velocities, an absolute minimum of three separate spectrophotometry sets must be available within 50 days of explosion.

If there were less than three available spectrophotometry sets before 50 days, and the linearity of θ/v continued beyond this epoch, we made an exception to the 50 day limit in using data sets after this time up to three data sets total. This exception was made for SN 2009N with Ba velocity, thus including a third data set 58 days postexplosion in our calculations.

Table 2 lists the SNe used in this study, with host-galaxy redshift from NED, estimated explosion time t_0, total E_{B-V}, and SN-specific photometry source articles. t_0 and E_{B-V} are obtained from the same source as photometry unless otherwise indicated. For the most part, abundant photometry was available in the *BVRI* bands for each supernova. All spectra were corrected for Milky Way extinction, host-galaxy extinction, and host-galaxy redshift before determining blackbody temperature and photospheric velocities.

4. Temperatures and Velocities

4.1. Blackbody Temperature

The angular radius of an SN photosphere is determined in part from the theoretical magnitude b and calculated flux dilution factor ζ in passband λ, both of which are dependent upon the photospheric temperature T (Equation (7)). Distance is then calculated from the ratio of the angular radius to the expansion velocity of the photosphere. For our calculations, we calculated the blackbody temperature of the photosphere based on a least-squares fit between the continuum spectrum and a Planck function of a Gaussian intensity curve (see Figure 1). Since a Planckian curve produces intensities several orders of magnitude larger than those of an observed SN spectrum, it must be normalized to the spectrum to maximize the fit.

Eastman et al. (1996) considered that the best-fit temperature might be dependent on wavelength, and observed that the fit appears to worsen as one shifts the wavelength range of the fit further away from the wavelength of peak emission. During the SN plateau phase, this peak usually occurs around 5000 Å. At shorter wavelengths, line blanketing makes it increasingly difficult to accurately fit a blackbody curve to the continuum. We tested blackbody fits in the wavelength range between 5200 and 6000 Å, which lies in a region of the visible spectrum that, for most SNe II, is relatively devoid of strong lines. This is close enough to the emission peak that we do not anticipate a serious issue. See the Appendix for more details about our procedure for fitting blackbody temperatures.

4.2. Line Velocities

Once the spectrum is corrected for the redshift of the SN's host galaxy, the intrinsic blueshift of a selected absorption line provides the line-specific velocity of the expanding ejecta by comparing its z-corrected absorption trough wavelength to its lab-frame wavelength. An absorption trough is identified by plotting the original spectrum file in the computing environment MATLAB, pinpointing the data point at the bottom of the trough, and using MATLAB's data cursor tool to identify its wavelength. If the trough is broad or flattened or noisy, data points at opposite edges of the trough provide a range of wavelengths from which a central wavelength and uncertainty are derived. For sharply defined troughs, a minimum uncertainty is taken to be half of the wavelength resolution of the spectrum. Uncertainty in the resulting line velocity is then a Gaussian propagation of the uncertainty in observed wavelength in the Doppler shift equation.

Early-time visible-light II-P spectra are nearly featureless except for weak Balmer lines and He I λ5876. The He I line disappears quickly while the Balmer lines get stronger, and as the plateau phase begins, Na I, Sc II, Ba II, Fe II, and other iron-group lines appear, along with strong line blanketing in the blue/UV (Filippenko 1997; Gutiérrez et al. 2017). Most of these lines, especially the stronger ones, have strong P-Cygni emission peaks, but it is the absorption trough that theoretically defines the direct line-of-sight photospheric velocity.

5. Analysis

To derive distances, we used Equation (7) to calculate θ separately for each passband in each spectrophotometry set, using ζ coefficients from both H01 and D05 for comparison. We then divided θ by a line-specific velocity v for that set, and plotted time t versus θ/v for that velocity. We then fitted a line to the individual data points up to 50 days postexplosion, and calculated the distance from its slope. Figures 2, 3, and 4 show examples of θ/v for SN 1999em, 2012ec, and 2009N. Data points plotted beyond 50 days show whether the linearity of θ/v changes or continues after this time.

Figure 5 shows the evolution of the blackbody temperature of SN 1999em, as calculated by our code. Note how our best-fit temperatures oscillate randomly during the plateau phase instead of remaining approximately steady. This probably explains the spread of θ/v values around the best-fit slopes for

[7] https://wiserep.weizmann.ac.il
[8] https://sne.space
[9] https://ned.ipac.caltech.edu

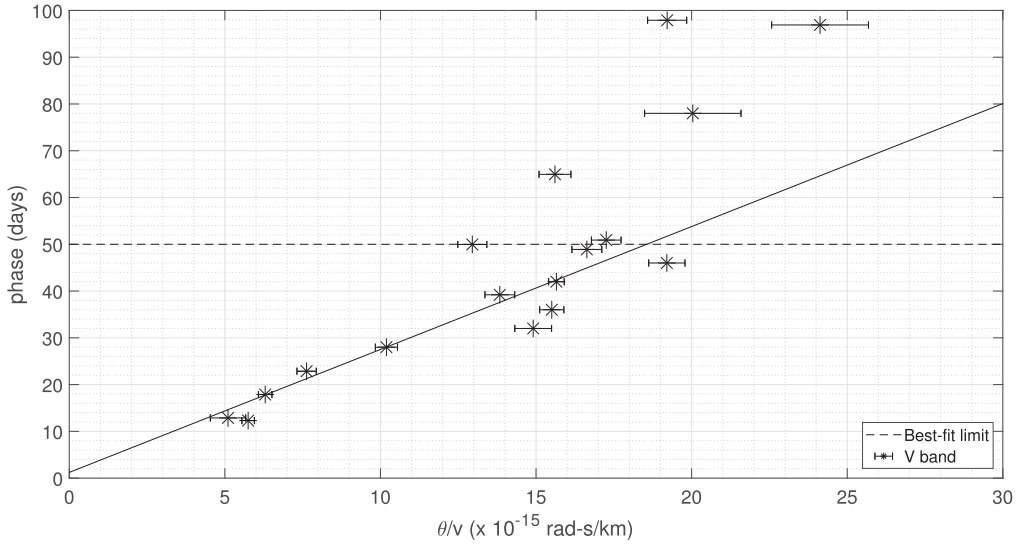

Figure 2. Time vs. θ/v for SN 1999em, using blackbody temperatures and the velocities derived from the Fe II 4924/5018/5169 triplet for passband *V*. Note that the slope is largely consistent up to approximately 50 days postexplosion (JD 2,451,529), indicated by the dashed line at 50 days.

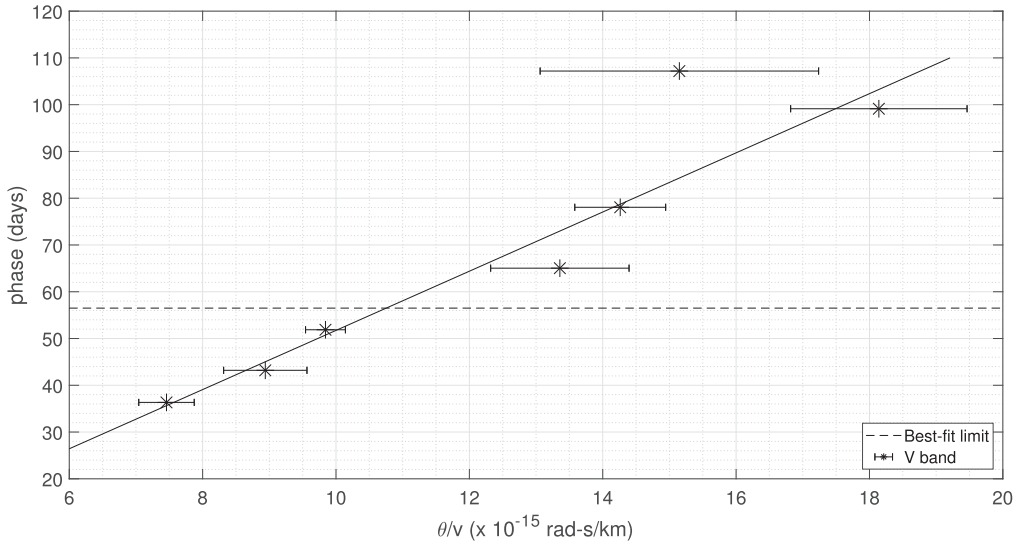

Figure 3. Time vs. θ/v for SN 2012ec, using blackbody temperature and the Sc velocity. Note that the slope appears consistent up to around 100 days postexplosion, but then "turns a corner" and becomes negative. The best-fit line was calculated for data sets up to approximately 56 days postexplosion.

all line species from 30 to 50 days postexplosion, despite the generally slow, steady declines in their velocities (see Figure 2 for iron).

Leonard et al. (2002a) noted that the Lick 1 m Nickel reflector showed continuum distortion at wavelengths of 5800 Å and greater in its spectra of SN 1999em. Such distortions would not necessarily affect the wavelengths of spectral lines but could affect the accuracy of blackbody temperature fits, resulting in apparent inconsistencies in an SN's temperature evolution. Our blackbody fits for the SN 1999em spectra at 10 and 11 days postexplosion produced especially low temperatures compared to spectra immediately before and after, and we omitted these spectra from our calculations. (We only measured Hβ and He velocities for these epochs.) Our blackbody fit for SN 2013ab at 31 days also gave an anomalously low temperature (Figure 6). We found no reference to continuum distortion in published literature for this supernova but nevertheless omitted this spectrum from our calculations.

Table 3 presents our EPM-derived distances for different line velocities in the *V* passband, using blackbody temperatures and H01's dilution correction factors. Table 4 is the same but uses D05's dilution factors. In both tables, we compare our results to the Tully–Fisher distances and the cosmology-corrected angular-size distance for the host galaxy, obtained from NED, and to EPM distances from previous studies where available. We additionally compare our distance to SN 1999em to Cepheid-derived distances. Results that are absent from the tables are cases where there is insufficient availability of data, or where the uncertainty in distance is larger than the distance itself. Note that the He line yielded few available results.

Overall, based on comparisons to alternate distance measurements and their relative uncertainties, our data suggest that Hβ, Fe II $\lambda\lambda$ 4924/5018/5169, and Ba II $\lambda\lambda$ 4554/5854/6142 are most likely to yield results that are in reasonable agreement with distances by other methods, including other EPM calculations, when using *V* photometry and blackbody temperature. A notable exception is that our Hβ and Fe II EPM

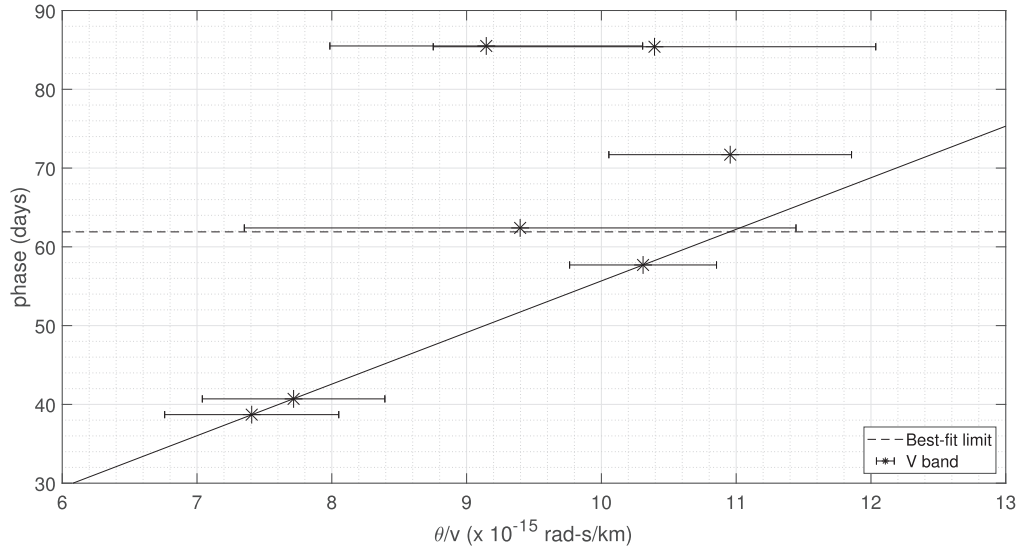

Figure 4. t vs. θ/v for SN 2009N, using blackbody temperature and the Ba II velocity. The linearity of the θ/v slope of the two available data sets within 50 days of explosion (up to JD 2,454,898) continues through a third data set at 58 days.

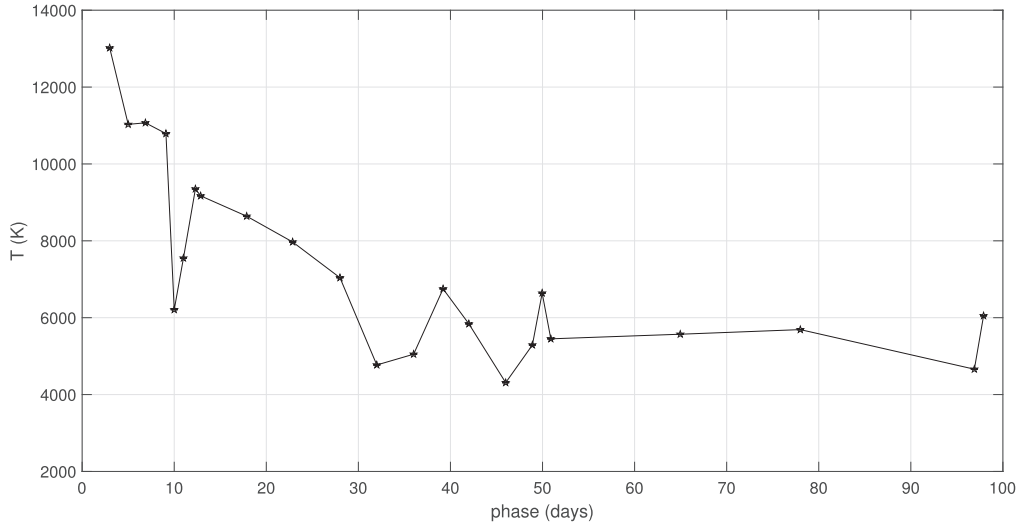

Figure 5. Plot of photospheric temperature of SN 1999em, as calculated by this work's blackbody fitting code, vs. time since explosion. Note how data points around 10 days and from 30 to 50 days show large deviations from a smoothly decreasing temperature.

distances to SN 2002gd, for which no other EPM distance has been published, are much larger than the angular-size and Tully–Fisher distances to its host galaxy.

Our data also support the findings of Jones et al. (2009) and Gall et al. (2018) that distances using D05's dilution correction factors are systematically larger than those using E96/H01 factors. One exception is that our Ba-velocity distance to SN 2009N using D05 is slightly smaller than that using H01. We further note that our data suggest that Fe II and Ba II distances agree a little better with distances by other methods if we use the D05 factors instead of H01. Interestingly, our Hβ distances appear to agree a little better when using the H01 factors. We observed that overall, for a chosen set of ζ coefficients, our Hβ distances are slightly larger than Fe distances when not comparable to them. The shorter distances of H01 factors compared to D05 apparently offset this difference. This observation does not necessarily take the uncertainties in these distances into enough account, and we note that the relative scatter of distances from different lines is substantially larger than that between the different dilution factors. Further study is warranted.

Leonard et al. (2002a) observed that using weak lines of Fe II $\lambda\lambda$4629/5276/5318 and Sc II λ4670 yielded velocities 8%–10% lower than those derived from Fe II $\lambda\lambda$4924/5018/5169. Using these line velocities and the E96 dilution factors, they obtained an EPM distance to SN 1999em of 8.2 ± 0.6 Mpc, which is comparable to other EPM distances, including our own. They noted that the systematic differences in distances between using E96 and H01 factors appeared to be small.

Jones et al. (2009) used Hβ velocities corrected for synthetic atmospheric models from E96 and D05 as well as their respective dilution factors to derive distances to SN 1999em of 9.3 ± 0.5 and 13.9 ± 1.4 Mpc, respectively. Their velocity correction factors predicted a significant difference between the Hβ velocity and the true photospheric velocity using the E96 atmospheric model, but very little difference using D05's model. Our Hβ distances were comparable to or slightly larger than our Fe distances despite being uncorrected in this way.

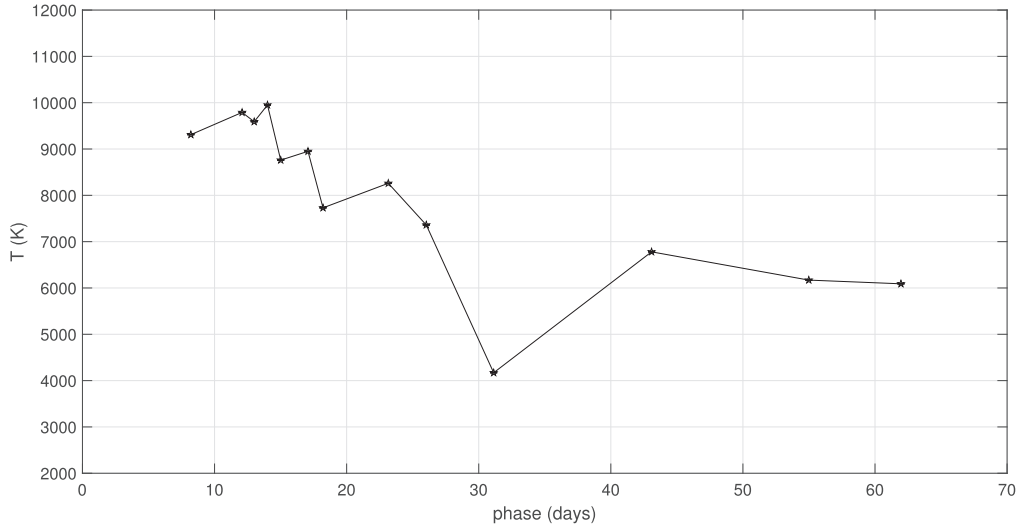

Figure 6. Plot of photospheric temperature of SN 2013ab, as calculated by this work's blackbody fitting code, vs. time since explosion. There is some dispersion from a smoothly decreasing temperature up to around 20 days, with a much larger deviation at 31 days.

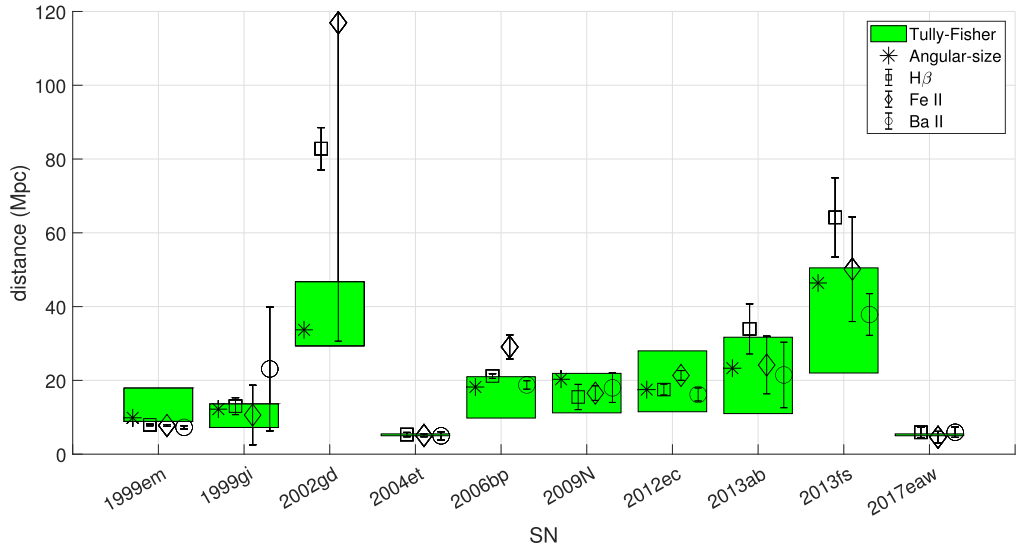

Figure 7. Graphical comparison of selected SN distances from Tables 3 and 4. Hβ distances use the H01 flux dilution factors, while Fe II and Ba II distances use the D05 factors. The upper and lower boundaries of the shaded areas show the range of Tully–Fisher distances for each SN.

Jones et al. (2009) noted that the linearity of θ/v did not necessarily remain constant for more than 50 days postexplosion (Section 2.2). Figure 2 shows this to be almost exactly the case for SN 1999em with Fe velocities. Similar results were seen for all other sampled velocities of SN 1999em, SN 1999gi, SN 2002gd, and SN 2017eaw, although there were long gaps in the available spectrophotometry sets of SN 1999gi and SN 2002gd after 40 days. We further observed that if calculations of θ/v are continued even further, the slope becomes negative, an example of which can be seen in Figure 3. We hypothesize that this occurs when the ejecta becomes diffuse enough, as it enters the nebular phase, that a thin photosphere can no longer be assumed. This typically begins around three months after the explosion (Filippenko 1997; Hamuy et al. 2001), long after EPM is considered no longer viable, and is indicated by a more rapid decline in overall brightness. We further hypothesize that a negative t versus θ/v slope indicates that the majority of flux by this time comes from layers receding so quickly into decreasing velocities that it makes the photosphere appear to be collapsing instead of expanding.

On the other hand, Figure 3 shows SN 2012ec with Sc velocity as an example of the initial linearity of θ/v continuing for almost 100 days after explosion. The linearity of the Hβ velocity also lasted almost 100 days for this supernova and at least 85 days for SN 2009N. The linearity of θ/v for SN 2004et continued for at least 75 days using Sc velocity. Otherwise, linearity for these three supernovae and for SN 2013ab continued up to 55–65 days for most velocities. Conversely, Ba in SN 2013ab appears to maintain linearity up to only 40–45 days postexplosion, although we note there were large uncertainties in θ/v for data sets around this epoch. We had no data sets beyond 50 days for SN 2006bp and SN 2013fs.

Figure 4 illustrates the case of SN 2009N with Ba velocity, where there were too few data sets available before 50 days but the linearity of the slope continued (Section 3). In Tables 3 and 4, we included the data set at 58 days postexplosion in our

Table 3
EPM Distances (Mpc) by Velocity, Using T_{bb}, V Passband, and ζ_{H01}

SN	Hβ This Work	He I This Work	Na I D This Work	Sc II This Work	Fe II This Work	Ba II This Work	EPM Other Sources	d_{angular}[a] NED	$d_{\text{Tully–Fisher}}$[b] NED
1999em	7.94 ± 0.21	7.42 ± 1.31	6.03 ± 0.41	5.01 ± 0.38	7.36 ± 0.23	6.60 ± 0.39	7.31 ± 0.10[d] 9.7 ± 0.8[e]	9.86	8.90–17.90 11.70–12.00[m]
1999gi	13.02 ± 2.31	⋯	⋯	⋯	9.86 ± 8.29	18.79 ± 11.61	$11.1^{+2.0}_{-1.8}$[f] 8.87 ± 0.34[g]	12.2	7.24–13.60
2002gd	82.81 ± 5.72	28.94 ± 6.81	⋯	⋯	95.85 ± 79.49	⋯	⋯	33.7	29.40–46.70
2004et	5.32 ± 0.57	⋯	6.88 ± 2.30	5.16 ± 2.12	4.30 ± 0.28	4.22 ± 1.01	4.02–5.86[e,g]	4.02–5.86[l]	4.99–5.50
2006bp	21.19 ± 0.63	24.87 ± 0.94	15.34 ± 1.02	16.53 ± 2.52	22.45 ± 2.38	14.88 ± 0.86	18.6 ± 1.5[e] 12.47 ± 0.57[g]	18.2	9.79–21.00
2009N	15.50 ± 3.42	⋯	11.59 ± 2.73	11.21 ± 1.70	14.19 ± 1.80	18.34 ± 4.76[c]	21.6 ± 1.1[h]	20.3	11.20–21.90
2012ec	17.51 ± 1.48	⋯	16.03 ± 3.78	17.72 ± 4.34	17.84 ± 1.10	13.53 ± 1.48	⋯	17.5	11.50–28.00
2013ab	33.96 ± 6.80	⋯	21.37 ± 3.41	⋯	19.87 ± 6.39	17.45 ± 7.06	24.26 ± 0.98[i] 18.64 ± 2.64[j]	23.3	11.00–31.70
2013fs	64.18 ± 10.77	33.98 ± 5.93	28.47 ± 16.61	13.44 ± 7.56	42.77 ± 12.39	31.89 ± 4.71	⋯	46.4	22.00–50.50
2017eaw	5.92 ± 1.44	11.26 ± 2.97	3.11 ± 0.94	2.33 ± 1.48	4.37 ± 1.61	5.09 ± 1.05	7.27 ± 0.42[k]	4.02–5.86[l]	4.99–5.50

Notes.
[a] Assuming $H_0 = 67.8$ km s^{-1} Mpc^{-1}, $\Omega_{\text{matter}} = 0.308$, and $\Omega_{\text{vacuum}} = 0.692$.
[b] See NED for original sources of Tully–Fisher distances.
[c] Using spectrophotometric data sets beyond 50 days postexplosion.
[d] Hamuy et al. (2001).
[e] Takats & Vinko (2012).
[f] Leonard et al. (2002a).
[g] Bose & Kumar (2014), using H01 correction factors.
[h] Takats et al. (2014).
[i] Bose et al. (2015).
[j] Müller et al. (2017).
[k] Van Dyk et al. (2019).
[l] No angular-size distance listed in NED. Distance range given is from previous EPM studies of SN 2004et in the same galaxy. (Takats & Vinko 2012; Bose & Kumar 2014).
[m] Cepheid distances.

Table 4
EPM Distances (Mpc) by Velocity, Using T_{bb}, V Passband, and ζ_{D05}

SN	Hβ This Work	He I This Work	Na I D This Work	Sc II This Work	Fe II This Work	Ba II This Work	EPM Other Sources	d_{angular}[a] NED	$d_{\text{Tully--Fisher}}$[b] NED
1999em	8.79 ± 0.26	9.34 ± 1.70	6.01 ± 0.38	5.10 ± 0.41	7.78 ± 0.25	7.27 ± 0.44	7.31 ± 0.10[d] 9.7 ± 0.8[e]	9.86	8.90–17.90 11.70–12.00[m]
1999gi	15.77 ± 2.98	⋯	⋯	⋯	10.61 ± 8.06	23.10 ± 16.77	$11.1^{+2.0}_{-1.8}$[f] 11.62 ± 0.29[g]	12.2	7.24–13.60
2002gd	106.75 ± 12.63	38.10 ± 9.67	⋯	⋯	116.93 ± 86.30	⋯	⋯	33.7	29.40–46.70
2004et	6.22 ± 0.67	⋯	7.46 ± 2.27	5.94 ± 2.15	5.07 ± 0.32	4.97 ± 1.12	4.02–5.86[e,g]	4.02–5.86[l]	4.99–5.50
2006bp	27.59 ± 0.90	31.08 ± 1.32	19.86 ± 1.46	21.07 ± 3.40	29.06 ± 3.28	18.76 ± 1.14	18.6 ± 1.5[e] 18.82 ± 1.04[g]	18.2	9.79–21.00
2009N	18.04 ± 3.83	⋯	13.64 ± 3.08	13.04 ± 1.91	16.55 ± 1.98	17.98 ± 3.96	21.6 ± 1.1[h]	20.3	11.20–21.90
2012ec	20.93 ± 1.78	⋯	18.87 ± 4.38	20.75 ± 5.02	21.34 ± 1.32	16.18 ± 1.77	⋯	17.5	11.50–28.00
2013ab	42.67 ± 9.01	⋯	26.21 ± 4.27	⋯	24.16 ± 7.79	21.47 ± 8.88	24.26 ± 0.98[i] 18.64 ± 2.64[j]	23.3	11.00–31.70
2013fs	78.20 ± 12.74	46.23 ± 9.21	33.52 ± 19.52	15.90 ± 8.88	50.14 ± 14.19	37.86 ± 5.65	⋯	46.4	22.00–50.50
2017eaw	6.75 ± 1.78	13.74 ± 3.72	3.44 ± 1.02	2.39 ± 1.35	4.60 ± 1.57	5.93 ± 1.39	7.27 ± 0.42[k]	4.02–5.86[l]	4.99–5.50

Notes.
[a] Assuming $H_0 = 67.8$ km s^{-1} Mpc^{-1}, $\Omega_{\text{matter}} = 0.308$, and $\Omega_{\text{vacuum}} = 0.692$.
[b] See NED for original sources of Tully–Fisher distances.
[c] Using spectrophotometric data sets beyond 50 days postexplosion.
[d] Hamuy et al. (2001).
[e] Takats & Vinko (2012).
[f] Leonard et al. (2002a).
[g] Bose & Kumar (2014), using D05 correction factors.
[h] Takats et al. (2014).
[i] Bose et al. (2015).
[j] Müller et al. (2017).
[k] Van Dyk et al. (2019).
[l] No angular-size distance listed in NED. Distance range given is from previous EPM studies of SN 2004et in the same galaxy. (Takats & Vinko 2012; Bose & Kumar 2014).
[m] Cepheid distances.

calculations to secure the minimum of three data sets for our requirements.

6. Summary

Our research appears to show that the EPM, using blackbody temperatures; Hβ, Fe II, and Ba II velocities; and the synthetic magnitudes of Hamuy et al. (2001) yield SN distances that are in reasonably good agreement with distances obtained by other methods. We found further evidence that the flux dilution factors of D05 yield systematically larger distances than the factors of H01. It is particularly significant that Hβ velocities, even without the corrections of Jones et al. (2009), appear to yield distances that are similar to those of Fe and Ba, since these lines do not appear in early-time spectra. One caveat here is that the agreement appears to be better if one uses the H01 factors for Hβ velocities while using the D05 factors for Fe and Ba. These results are displayed in Figure 7.

We obtained EPM distances for three new SNe, SN 2002gd, SN 2012ec, and SN 2013fs. Our results for the latter two, using Hβ, Fe, and Ba, are in reasonably good agreement with Tully–Fisher and angular-size distances to their respective host galaxies, using either set of dilution factors; however, our distances for 2002gd are much larger than Tully–Fisher and angular-size. Further study is needed to investigate if this might be due to some intrinsic property of the supernova or its environment, although we note that the range of our Fe distance, due to its very large uncertainty, does include both Tully–Fisher and angular-size.

We note that the period over which θ/v yields a linear slope necessary for good results in EPM can vary from SN to SN and even over different line velocities. In most such cases, this only extends the expected 50 day duration of linearities up to around 60 days, but we observed four specific cases where linearity appeared to last 75–100 days (SN 2004et, Sc; SN 2009N, Hβ; SN 2012ec, Hβ and Sc). Could there be physical reasons for this within the ejecta? Future research will sample more SNe to further test the efficacy of Hβ, Fe II, and Ba II velocities, and search for possible trends in the duration of θ/v linearity for different SNe. We also intend to compare results using different methods of determining temperature—blackbody temperature versus color temperature—in Paper II of this series.

In Section 2.2, we noted that the ζ coefficients of Hamuy et al. (2001) and Dessart & Hillier (2005) were specific to Type II-P SNe. Dessart et al. (2015) attempted to derive coefficients for stripped-envelope SNe (Types IIb, Ib, and Ic). Bearing in mind that the asphericity of the inner layers of ejecta (Wang & Wheeler 2008) is likely to appear at earlier times for these SNe, we plan to test Dessart et al.'s (2015) coefficients in a future study.

This research has made use of the NASA/IPAC Extragalactic Database (NED; 10.26132/NED1), which is operated by the Jet Propulsion Laboratory, California Institute of Technology, under contract with the National Aeronautics and Space Administration.

We gratefully acknowledge the additional support of St. Ambrose University's donor-funded Undergraduate Summer Research Institute, the MATLAB suite for our calculations, and the Weizmann Interactive Supernova Data Repository (WISeREP) and Open Supernova Catalog for providing our spectra. We also acknowledge the SAO/NASA Astrophysics Data System, operated by the Smithsonian Astrophysical Observatory under NASA Cooperative Agreement NNX16AC86A, for locating references that provided photometry and other data on our supernovae.

Appendix

Considering the possibility that the best-fit temperature might depend on what specific wavelength we use to normalize the blackbody curve (Eastman et al. 1996), we created a code that calculates the chi-squared between a continuum spectrum and the normalized Planckian curve with two parameters, temperature and normalization wavelength, confining our wavelength range between 5200 and 6000 Å, as described in Section 4.1.

We tested this code with two spectra from each of the SNe in our sample. An example of the results can be seen in Figure 8 as a 3D graph of chi-squared versus temperature versus normalization wavelength. We observed that, in all cases, chi-squared is much less sensitive to wavelength than to temperature. Figure 9 is a 2D cross section of Figure 8 showing only chi-squared versus temperature.

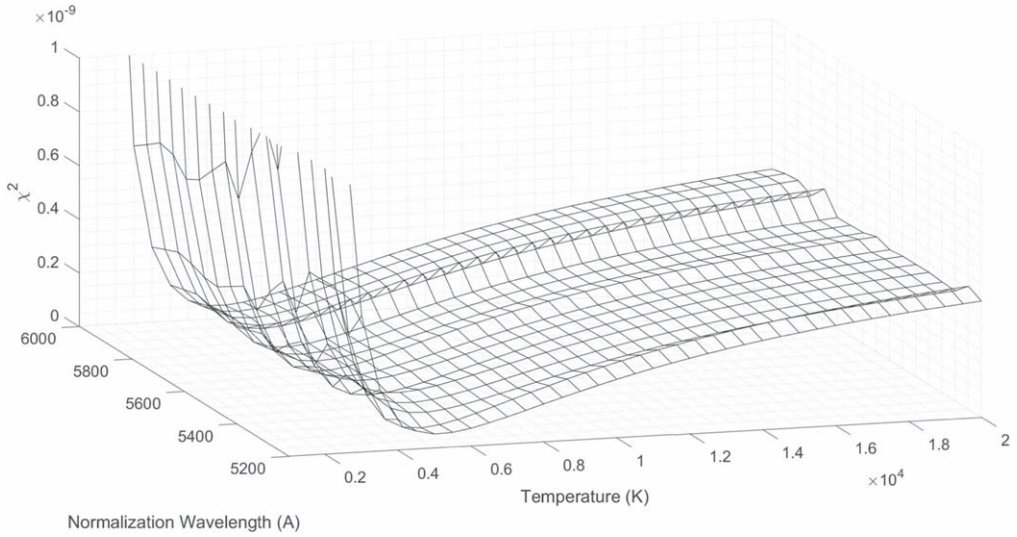

Figure 8. Chi-squared vs. normalization wavelength and blackbody temperature for the 2017 July 13 spectrum of SN 2017eaw. Chi-squared is much more dependent on temperature.

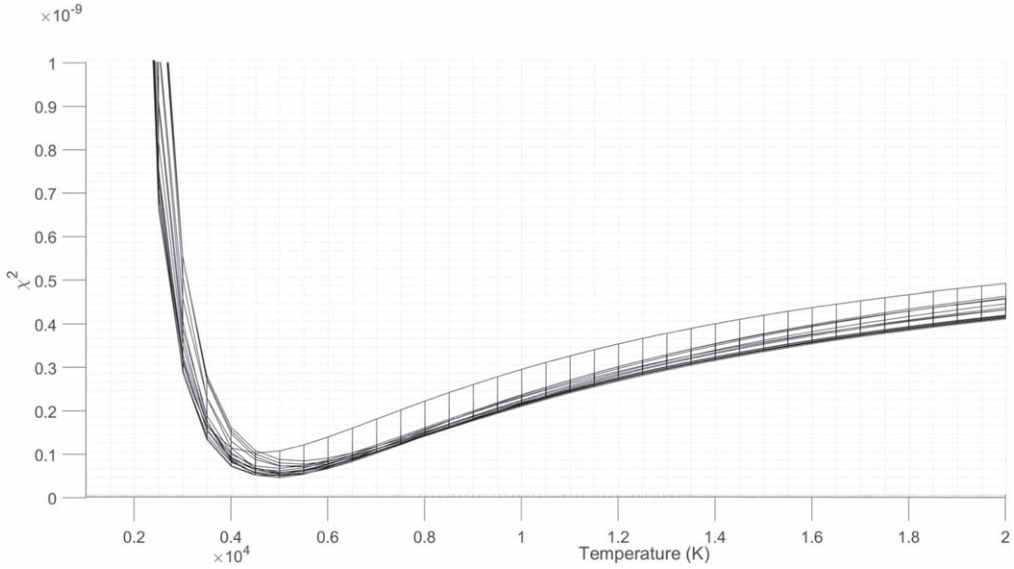

Figure 9. Chi-squared vs. blackbody temperature for the 2017 July 13 spectrum of SN 2017eaw.

ORCID iDs

R. C. Mitchell https://orcid.org/0000-0002-9015-3099

References

Baade, W. 1926, AN, 228, 359
Barbarino, C., Dall'Ora, M., Botticella, M. T., et al. 2015, MNRAS, 448, 2313
Bose, S., & Kumar, B. 2014, ApJ, 782, 98
Bose, S., Valenti, S., Misra, K., et al. 2015, MNRAS, 450, 2373
Burstein, D., & Heiles, C. 1982, AJ, 87, 1165
Couch, S. M., Wheeler, J. C., & Milosavljević, M. 2009, ApJ, 696, 953
Dessart, L., Blondin, S., Brown, P. J., et al. 2008, ApJ, 675, 644
Dessart, L., & Hillier, D. J. 2005, A&A, 439, 671
Dessart, L., Hillier, D. J., Woosley, S., et al. 2015, MNRAS, 453, 2189
Dong, Y., Valenti, S., Bostroem, K. A., et al. 2021, ApJ, 906, 56
Eastman, R. G., & Kirshner, R. P. 1989, ApJ, 347, 771
Eastman, R. G., Schmidt, B. P., & Kirshner, R. P. 1996, ApJ, 466, 911
Filippenko, A. V. 1997, ARA&A, 35, 309
Fitzpatrick, E. L. 1999, PASP, 111, 63
Gall, E. E. E., Kotak, R., Leibundgut, B., et al. 2018, A&A, 611, A25
Guillochon, J., Parrent, J., Kelley, L. Z., et al. 2017, ApJ, 835, 64
Gutiérrez, C. P., Anderson, J. P., Hamuy, M., et al. 2017, ApJ, 850, 89
Hamuy, M., Pinto, P. A., Maza, J., et al. 2001, ApJ, 558, 615
Jeffery, D. J., & Branch, D. 1989, in Supernovae: Jerusalem Winter School for Theoretical Physics, ed. J. C. Wheeler, T. Piran, & S. Weinberg, Vol. 6 (Singapore: World Scientific), 149
Jones, M. I., Hamuy, M., Lira, P., et al. 2009, ApJ, 696, 1176
Kirshner, R. P., & Kwan, J. 1974, ApJ, 193, 27
Leonard, D. C., Filippenko, A. V., Ganeshalingam, M., et al. 2006, Natur, 440, 505
Leonard, D. C., Filippenko, A. V., Gates, E. L., et al. 2002b, PASP, 114, 35
Leonard, D. C., Filippenko, A. V., Weidong, L., et al. 2002a, AJ, 124, 2490
Maeda, K., Nakamura, T., Nomoto, K., et al. 2002, ApJ, 565, 405
Müller, T., Prieto, J., Pejcha, O., & Clocchiatti, A. 2017, ApJ, 841, 127
Nagao, T., Cikota, A., Patat, F., et al. 2019, MNRAS, 489, L69
Nugent, P., Sullivan, M., Ellis, R., et al. 2006, ApJ, 645, 841
Petrushevska, T. 2020, Symm, 12, 1966
Quimby, R. M., Wheeler, J. C., Höflich, P., et al. 2007, ApJ, 666, 1093
Sahu, D. K., Anupama, G. C., Srividya, S., & Muneer, S. 2006, MNRAS, 372, 1315
Schmidt, B. P., Kirshner, R. P., & Eastman, R. G. 1992, ApJ, 395, 366
Schmidt, B. P., Kirshner, R. P., Eastman, R. G., et al. 1994, AJ, 107, 1444
Smartt, S. J. 2015, PASA, 32, e016
Smartt, S. J., Eldridge, J. J., Crockett, R. M., & Maund, J. R. 2009, MNRAS, 395, 1409
Spiro, S., Pastorello, A., Pumo, M. L., et al. 2014, MNRAS, 439, 2873
Szalai, T., Vinkó, J., Könyves-Tóth, R., et al. 2019, ApJ, 876, 19
Takats, K., Pumo, M. L., Elias-Rosa, N., et al. 2014, MNRAS, 438, 368
Takats, K., & Vinko, J. 2012, MNRAS, 419, 2783
Valenti, S., Howell, D. A., Stritzinger, M. D., et al. 2016, MNRAS, 459, 3939
Van Dyk, S. D., Zheng, W., Maund, J. R., et al. 2019, ApJ, 875, 136
Vinkó, J., & Takáts, K. 2007, in AIP Conf. Proc. 937, SUPERNOVA 1987A: 20 YEARS AFTER: Supernovae and Gamma-Ray Bursters (Melville, NY: AIP), 394
Wang, L., & Wheeler, J. C. 2008, ARA&A, 46, 433
Yan, H., Ma, Z., Ling, C., et al. 2023, ApJL, 942, L9
Yaron, O., & Gal-Yam, A. 2012, PASP, 124, 668